PAPER

Check for updates

Removal of *p*-nitrophenol from simulated sewage using MgCo-3D hydrotalcite nanospheres: capability and mechanism

Fei Gao, [ID] Xinru Xu and Jingyi Yang*

4-Nitrophenol (4-NP) is an organic pollutant found in the wastewater discharged from coking and petrochemical industries, and it is highly toxic, persistent, and bioaccumulative. 4-NP is difficult to degrade and causes serious damage to human health and the ecological environment. In this study, MgCo-3D hydrotalcite nanospheres were synthesized *via* the hot solvent method using ZIF-67 as a template for 4-NP removal from wastewater. The composition and structure of MgCo-3D hydrotalcite nanospheres were characterized *via* X-ray diffraction (XRD), Scanning electron microscope (SEM), Transmission Electron Microscope (TEM), Fourier-transform infrared spectroscopy (FT-IR), X-ray photoelectron spectroscopy (XPS), Energy Dispersive Spectroscopy (EDS), and BET analyses. The maximum adsorption capacity was 131.59 mg g^{-1} under the optimized conditions (pH = 7, t = 298 K, C_0 = 50 mg L^{-1}, dose = 0.4 g L^{-1}). The adsorption obeyed the Langmuir, Redlich–Peterson and Sips models and pseudo-second-order kinetics, and the adsorption activation energy was 29.4 kJ mol^{-1}, indicating a monolayer physical adsorption phenomenon. The adsorption of 4-NP on the MgCo-3D hydrotalcite nanospheres mainly involved hydrogen bonding and electrostatic interactions. The nanospheres were regenerated using the hot-air purging method. After five adsorption–desorption cycles, the adsorption capacity reached 107.6 mg g^{-1}, indicating the good regeneration performance of the MgCo-3D hydrotalcite nanospheres.

1. Introduction

4-Nitrophenol (4-NP) is a bioaccumulative, persistent, highly toxic, and non-degradable pollutant, mainly from the sewage discharge of coal, petrochemical, and steel industries.[1] The maximum concentration of 4-NP in wastewater should not exceed 1 ppm (mg kg^{-1}).[2,3] The removal of *p*-nitrophenol from wastewater mainly includes membrane separation, precipitation, redox reactions, and biological methods.[4,5] Among them, the adsorption method is widely used because it is safe, efficient, and operationally simple.[6,7]

Layered double hydroxides (LDHs) are suitable for wastewater treatment. Sun[8] and Balbino[9] synthesized some two-dimensional (2D) layered hydrotalcites for high adsorption capacity of 4-NP, however, they have certain limitations. For example, 2D hydrotalcite nanosheets gradually stack during synthesis, which significantly reduces the surface area and thus the number of active sites. This undesirable agglomeration of nanosheets can be circumvented in three-dimensional (3D) hydrotalcites.[10–12]

Metal–organic frameworks (MOFs) are coordination polymers with a 3D pore structure, which have high porosity, large

East China University of Science and Technology School of Chemical Engineering, China. E-mail: jyyang@ecust.edu.cn

specific surface area, high chemical stability and abundant unsaturated coordination sites rendering them effective adsorbents.[13–15] Miao *et al.*[16] synthesized a silver(ı) 3,5-diphenyl-triazolate MOF, AgTz-1, that exhibited a maximum adsorption capacity of 143.5 mg g^{-1} for 4-NP. Aldawsari *et al.*[17] developed a class of porous adsorbent composite, AC-NH2-MIL-101 (Cr), which adsorbed 4-NP with a capacity of 183 mg g^{-1}. Lin *et al.*[18] synthesized a copper-based MOF (HKUST-1) with an adsorption capacity of up to 400 mg g^{-1}. However, the cost and recycling of MOF powder limits its application in industry.

Therefore, researchers focus on developing more feasible cost-effective adsorbents. Hydrotalcite synthesized with a MOF as a template not only has a three-dimensional structure, but also can reduce the cost and increase the surface area of the adsorbents. ZIF-67, a type of MOF material, can be used to synthesize a 3D hydrotalcite template.[19,20] In previous studies, hydrotalcite materials synthesized using MOFs as a template were mostly used for catalytic oxidation, fabrication of capacitors, *etc*[21–24]. Studies on LDH/MOF interactions or adsorption mechanisms in wastewater are still limited, and further investigations are required.

In this study, a MgCo-3D hydrotalcite adsorbent was synthesized using ZIF-67 as a template to remove 4-NP from simulated wastewater by intermittent adsorption. The adsorption performance was evaluated using kinetic, isothermal, and

thermodynamic models to elucidate the adsorption mechanism. The adsorbent was investigated by XRD, FT-IR spectroscopy, and XPS. The effect of pH and ionic strength and the regeneration performance of the adsorbent were also studied. The results suggest that MgCo-3D hydrotalcite nanospheres can be used as an efficient adsorbent for 4-NP.

2. Experimental methods

2.1 Materials

2-Methylimidazole, 4-NP, and methanol (analytical grade) were purchased from Beijing Bailingway Technology Co., Ltd. Hexahydrate magnesium nitrate (analytical grade) and sodium hydroxide (analytical grade) were purchased from Shanghai Titan Co., Ltd. and cobalt nitrate hexahydrate (analytical grade) was purchased from Shanghai Maclean Biochemical Technology Co., Ltd.

2.2 Preparation of MgCo-3D hydrotalcite nanospheres

2.2.1 Synthesis of ZIF-67 nanocrystals. ZIF-67 nanocrystals were prepared as follows: 6.56 g of 2-methylimidazole and 5.82 g of $Co(NO_3)_2$–$6H_2O$ were weighed and separately dissolved in 400 mL of anhydrous methanol. The $Co(NO_3)_2$–$6H_2O$ solution was slowly poured into a stirred 2-methylimidazole solution, and the stirring was stopped after 24 h. The solution was centrifuged, and the residue was washed thrice with anhydrous methanol and dried at 70 °C.

2.2.2 Synthesis of MgCo-3D hydrotalcite nanospheres derived from ZIF-67. MgCo-3D hydrotalcite was prepared using a hydrothermal method. Briefly, 43.3 mg of magnesium nitrate hexahydrate and 24 mg ZIF-67 were added in 60 mL of anhydrous ethanol, and the mixture was sonicated for 10 min. The mixed solution was then transferred to a polytetrafluoroethylene reactor and allowed to react at 120 °C for 6 h. Subsequently, it was washed three times with anhydrous ethanol and dried at 70 °C.[22]

2.3 Characterization

Morphologies were observed by SEM (Nova Nano SEM 450, EFI, USA), in conjunction with energy-dispersive X-ray spectroscopy (EDS). The structure and composition were analyzed by XRD. XRD patterns were recorded on a D8 Advance X-ray diffractometer using Cu Kα radiation At a tube voltage of 40 kV, tube current of 100 mA, the scan range of 5°–90°, scan rate 10° per min, and scan step 0.01°, FT-IR spectroscopy (Nicolet 6700, Thermo Fisher Scientific, USA) and XPS (K-alpha, Thermo Scientific, USA) were used to analyze the functional groups and surface chemical state of the MgCo-3D hydrotalcite nanospheres. The N2 adsorption–desorption isotherms and specific surface area of the MgCo-3D hydrotalcite nanospheres were evaluated using automatic volumetric adsorption equipment (Micromeritics, ASAP2460, USA). The zeta potentials of the MgCo-3D hydrotalcite nanosphere surfaces at different pH values (3–13) were measured using a laser particle size analyzer (McChik, Microtrac S3500SI, USA).

2.4 Batch adsorption experiment

A 4-NP solution (50 mg L^{-1}) was prepared in a volumetric flask. Next, 0.01 g of the adsorbent was mixed with 30 mL of the 4-NP solution in a 50 mL Erlenmeyer flask fitted with a rubber stopper. The mixture was shaken at 150 rpm in a bench-type thermostatic oscillator (SHA-B, Suzhou Guofei Laboratory Instrument Co., Ltd.) for 1 h. Samples (3 mL) were removed from the suspension and passed through a 0.22 μm disposable water-phase needle filter. The concentration of 4-NP in the sample was measured using a UV spectrophotometer at a wavelength of 310 nm.

The adsorption capacity of the hydrotalcite at any time was calculated using eqn (1):

$$q_t = \frac{(C_0 - C_t) \times V}{m} \tag{1}$$

Here, q_t (mg g^{-1}) is the amount of 4-NP adsorbed by the MgCo-3D hydrotalcite nanospheres at time t, C_0 and C_t (mg L^{-1}) are the initial and residual 4-NP in solution at time t, respectively, V (L) is the volume of the 4-NP solution, and m (g) is the weight of the adsorbent.

2.5 Regeneration experiment

The saturated adsorbent was obtained by centrifuging the suspension after the batch adsorption experiment and then purge the wet solid adsorbent in hot air for regeneration. The saturated adsorbent was purged with hot air at 200 °C for 4 h at an airflow rate of 4 L min^{-1}. The reusability of the adsorbents was investigated for five cycles under the same conditions.

3. Results and discussion

3.1 Characterization of synthesized products

The XRD pattern of the MgCo-3D hydrotalcite nanospheres is shown in Fig. 1(a). The sample exhibited characteristic hydrotalcite peaks at $2\theta = 11°$, 23°, and 60°, corresponding to the d (003), d (006), and d (110) crystal planes; this indicated the
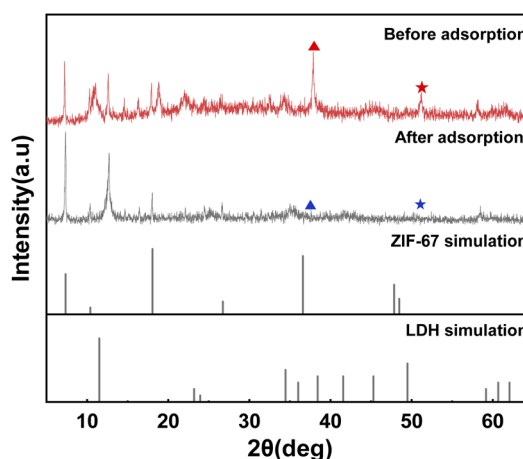

Fig. 1 XRD patterns before and after adsorption.

successful preparation of the hydrotalcite. In addition to the hydrotalcite peak, characteristic peaks were observed at $2\theta = 7.2°$, $10.4°$, $18°$, $26.7°$, and $36.3°$, corresponding to the d (110), d (002), d (222), d (134), and d (444) crystal planes of ZIF-67.[25] This suggested that the ZIF-67 template was retained during the synthesis. These results suggested that the MgCo-3D hydrotalcite composite retained the properties of LDHs. Therefore, the MgCo-3D hydrotalcite composites can effectively adsorb 4-NP contaminants.[26]

The morphology of the MgCo-3D hydrotalcite nanospheres was observed by SEM (Fig. 2(b)). After the hydrothermal treatment, the resulting MgCo-3D hydrotalcite nanospheres were adhesively grafted onto ZIF-67, inheriting the rhombic dodecahedral morphology of ZIF-67 (Fig. 2(a)).[27] The specific structure of the MgCo-3D hydrotalcite nanospheres was further investigated by TEM. TEM analysis revealed that the particle size of the hydrotalcite sample was approximately the same as that of ZIF-67 (Fig. 2(c)) and that the MgCo-3D hydrotalcite

nanospheres were wrapped around ZIF-67 as a thin sheet. The three-dimensional structure of hydrotalcite changes the agglomeration of hydrotalcite flakes, also providing convenient conditions for 4-NP. The elemental surface distributions of the adsorbents were determined separately *via* EDS analysis (Fig. 2(d and e)), which revealed that Mg and Co were uniformly distributed on the surface.

The surface area and pore structure are important factors affecting the adsorption performance. Consequently, the N2 adsorption–desorption isotherms (Fig. 3(a)) of the material were acquired after degassing the samples at 150 °C for 6 h. The adsorption–desorption curves were consistent with a type IV isotherm, indicating the presence of mesopores in the samples.[28] Thus, the micropores of ZIF-67 changed to mesopores in the prepared adsorbent due to the growth of nanosheets on the surface of the polyhedral, resulting in the transformation of the porous MOF into a hierarchically structured nanosheet material. The isotherm of MgCo-3D
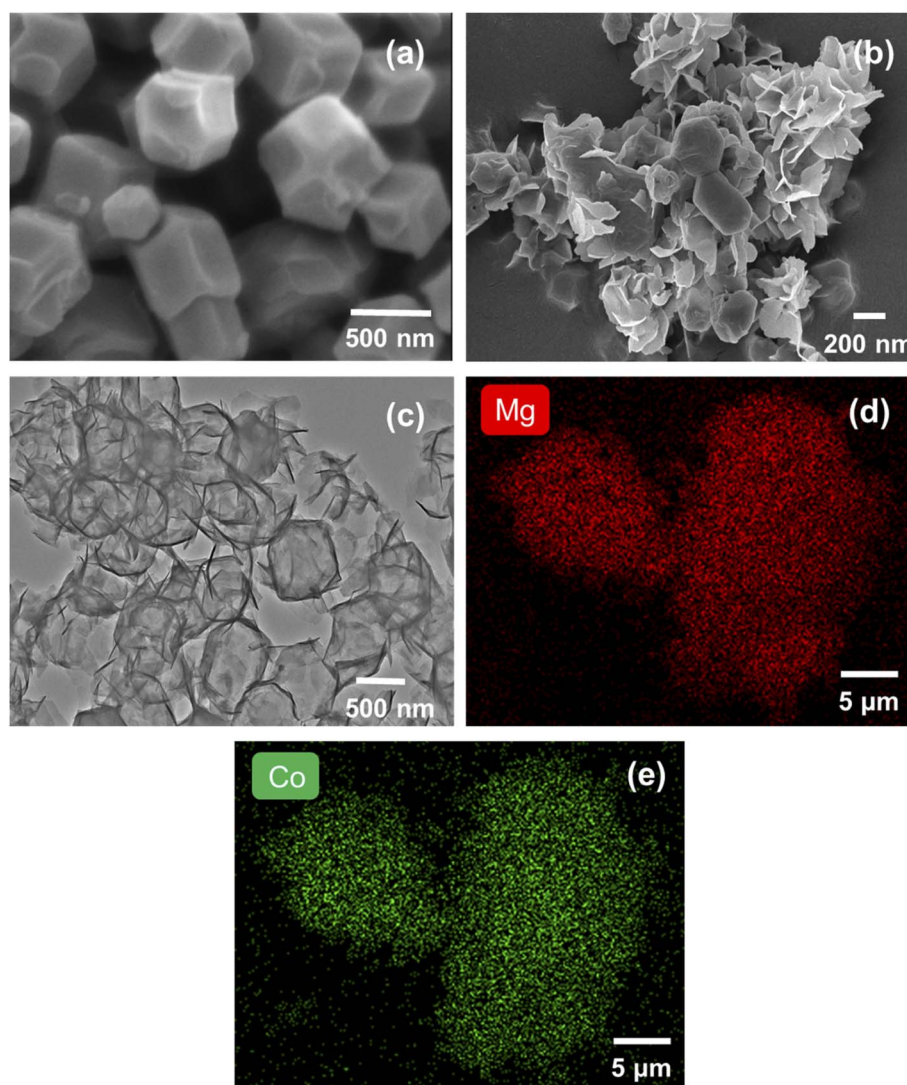

Fig. 2 (a) SEM image of ZIF-67. (b) SEM image of MgCo-3D hydrotalcite. (c) TEM images of MgCo-3D hydrotalcite. (d and e) EDS analysis and electron mapping of MgCo-3D hydrotalcite.
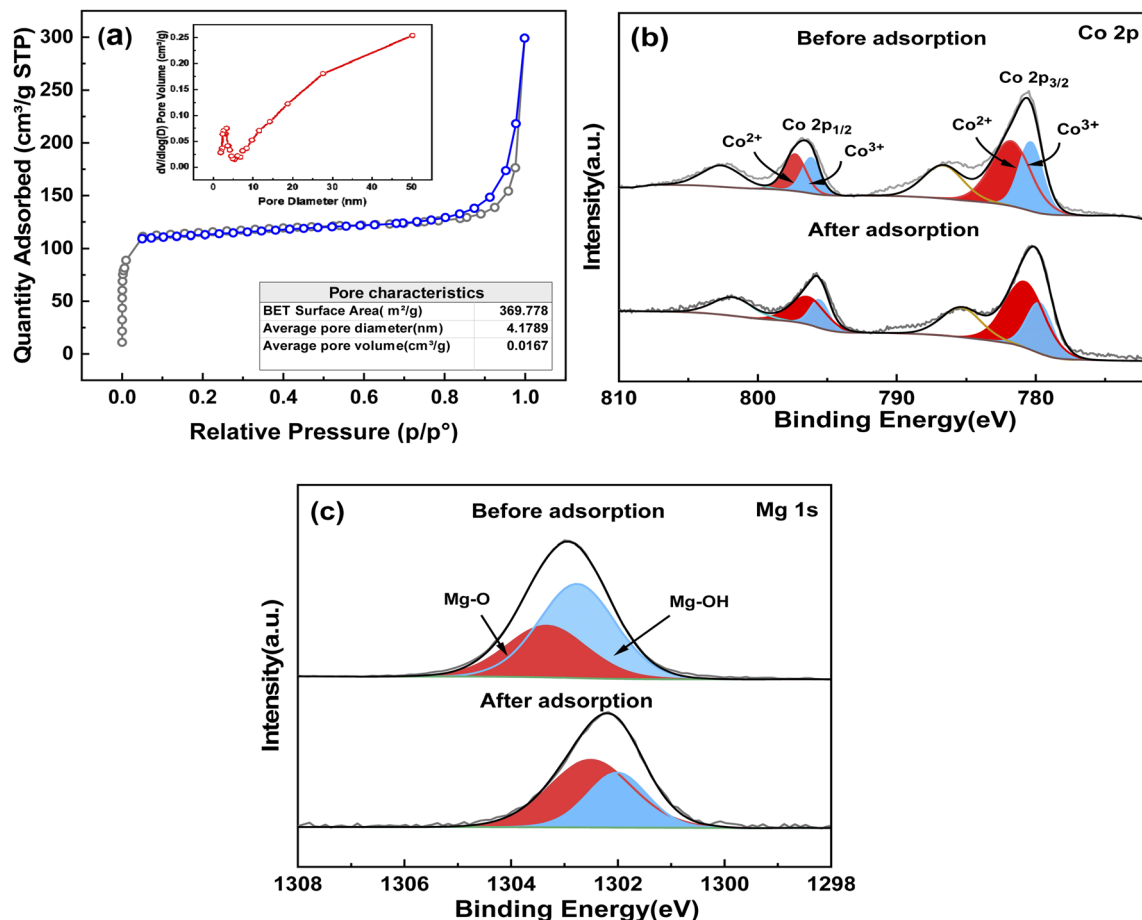
Fig. 3 (a) N_2 adsorption–desorption isotherms and pore size distribution of the MgCo-3D hydrotalcite nanospheres. (b) Co 2p and (c) Mg 1s XPS fine spectra of the MgCo-3D hydrotalcite nanospheres before and after adsorption.

hydrotalcite was indicative of an H4 hysteresis loop ($P/P_0 > 0.8$), which corresponds to a slit pore. This is distinguished by particle stacking, wherein some pores are similar to those produced by lamellar structures. Additionally, no saturated adsorption platform is observed, indicating an irregular pore structure. The BET surface area of MgCo-3D hydrotalcite is 369.78 m^2 g^{-1}, which is much larger than those of other two-dimensional hydrotalcite materials. As the surface area increases, the active sites increase, so the adsorption capacity is also improved compared with the traditional hydrotalcite. Using the BJH equation, the pore size of the MgCo-3D hydrotalcite was calculated to be 4.18 nm.[29]

To further determine the atomic and electronic structures of the MgCo-3D hydrotalcite surface, the adsorbent was subjected to XPS analysis, which was performed based on the residual carbon (standard position at 284.6 eV). The Co 2p and Mg 1s spectra of the MgCo-3D hydrotalcite nanospheres are shown in Fig. 3(b and c). The Co 2p spectrum showed two main peaks (2p3/2 at 780.6 eV and 2p1/2 at 796.8 eV). Deconvolution of the spectrum revealed peaks at 779.90 and 796.16 eV, corresponding to Co3+ and at 781.5 and 797.33 eV, corresponding to Co2+. This confirmed the partial oxidation of Co2+ to Co3+. These Co 2p and Mg 1s (1302.28 eV) peaks supported the formation of the MgCo-3D hydrotalcite nanospheres.[30]

3.2 Batch adsorption experiment

3.2.1 Effect of time and temperature. Time and temperature are important factors determining the adsorption performance. Therefore, the adsorption equilibrium time and adsorption efficiency of the MgCo-3D hydrotalcite nanospheres at different temperatures were examined (Fig. 4(a)). The maximum adsorption capacity was 131.59 mg g^{-1} at 298 K and pH 7, at an initial concentration of 50 mg L^{-1} and dose 0.4 g L^{-1}. The adsorption capacity increased gradually with time, with rapid adsorption in the initial stage (0–3 min). The adsorption rate decreased gradually as the adsorption sites were occupied, reaching equilibrium within 5 min. The adsorption capacities of different adsorbents for 4-NP are listed in Table 1. Notably, the adsorption capacity slightly changed when the temperature was increased to 318 K. "However, the adsorption rate of the material increased with increasing temperature, indicating that higher temperatures increased the thermal motion of 4-NP, thereby lowering the time required to attain equilibrium.

3.2.2 Effect of pH and ion concentration. pH is also an important parameter in the adsorption of 4-NP. The pH of the 4-NP solution was adjusted to 3–13 (50 mg L^{-1}) using 0.1 mol L^{-1} hydrochloric acid and sodium hydroxide solutions, and the
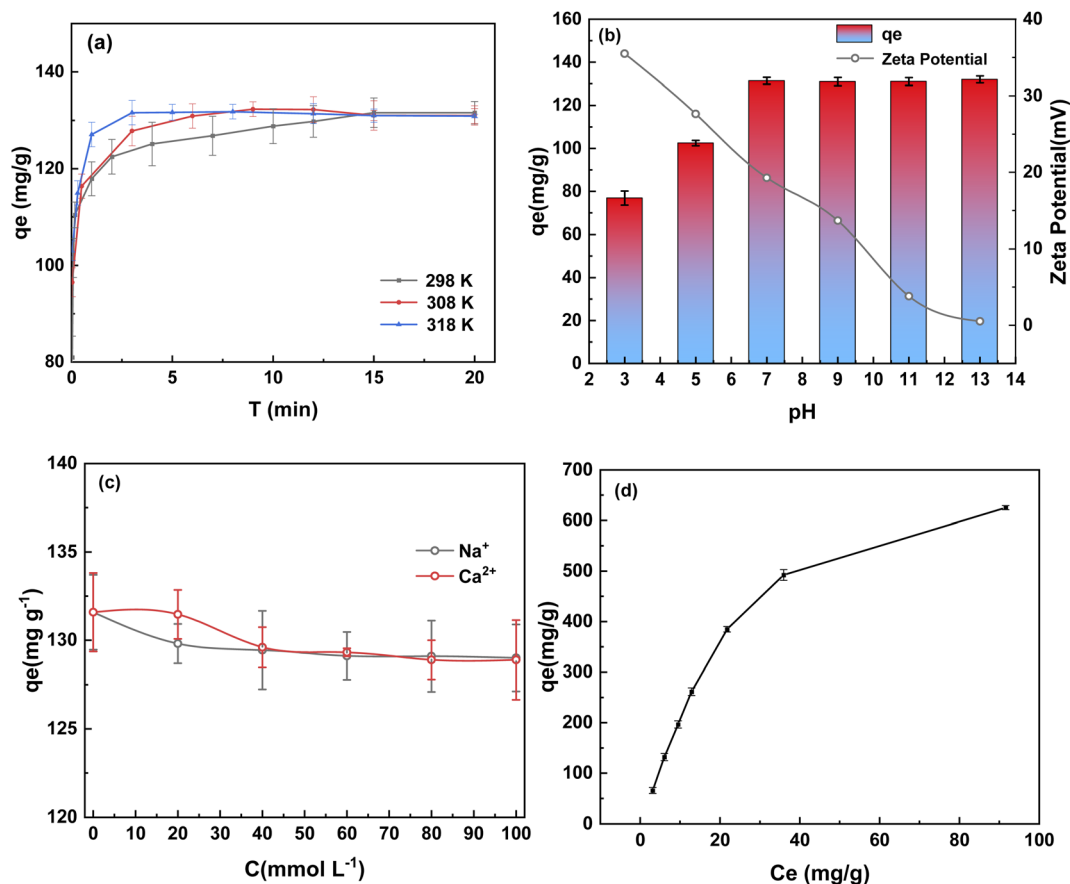
Fig. 4 (a) Effect of time and temperature (experimental conditions: $C_0 = 50$ mg L^{-1}; dose = 0.4 g L^{-1}; $t = 60$ min; $T = 298$, 308, and 318 K). (b) Effect of pH on the adsorption of 4-NP (experimental conditions: $C_0 = 50$ mg L^{-1}; $T = 298$ K; dose = 0.4 g L^{-1}; $t = 60$ min) and zeta potential of MgCo-3D hydrotalcite nanospheres at different pH values. (c) Effect of ionic strength on adsorption (Na$^+$, Ca^{2+}). (d) Effect of initial concentration (Ce (mg g^{-1})) of 4-NP (25–300 mg L^{-1}) at equilibrium.

adsorption capacity and zeta potential of the adsorbent at different pH values were measured (Fig. 4(b)). At low pH values, H$^+$ ions protonated the hydroxyl groups of the LDH layer to form water,[31] resulting in the loss of the active center and hence a decrease in the adsorption capacity. The adsorption capacity reached its maximum at pH 7 and only slightly changed beyond this pH.

Coking industrial wastewater contains common ions that may competitively bind to or occupy the available sites. To further evaluate the adsorption selectivity of the MgCo-3D

hydrotalcite nanospheres for 4-NP, the effect of Na$^+$ and Ca^{2+} ions on the adsorption capacity was investigated by mixing 0–100 mmol NaCl and CaCl$_2$ with 50 mg of a 4-NP solution. The results are shown in Fig. 4(c). The adsorption capacity decreased from 131 to 128.89 mg g^{-1} and 129.00 mg g^{-1} when the coexisting ion concentration was 100 mmol L^{-1}. No further change in the adsorption capacity was observed with increasing ion concentration. This is probably because the positive charge in the adsorbent surface repels the Na$^+$ and Ca^{2+} ions, owing to which these ions do not compete for adsorption.[32]

Table 1 Adsorption capacity of 4-NP on different adsorbents

Material	Adsorption capacity	Ref.
Corn husk	7.936 mg g^{-1}	34
Microalgal biochar	204.8 mg g^{-1}	35
Silver(I) 3,5-diphenyltriazolate MOF–AgTz-1	184.8 mg g^{-1}	36
AC-NH2-MIL-101(Cr)	183 mg g^{-1}	37
Amino-MIL-53(Al)	297.85 mg g^{-1}	38
CaAl-LDH/g-CN@Fe$_3$O$_4$ NC	550 mg g^{-1}	39
CD@Si	41.5 mg g^{-1}	40
Organoclays	14.286 mg g^{-1}	41
MgCo-3D hydrotalcite nanospheres	131.59 ± 2.34 mg g^{-1}	This work

3.2.3 Effect of initial concentration. To examine the effect of initial concentration, 0.01 g of the adsorbent was added to 30 mL of 25–300 mg L^{-1} 4-NP solution at 25–45 °C and pH 7. Fig. 4(d) shows that the adsorption capacity gradually increased with increasing 4-NP concentrations. The usual concentration of phenolic compounds in industrial wastewaters, such as those from coking plants and comprehensive oil refining plants, is 40–80 mg L^{-1}.[33] Thus, 50 mg L^{-1} was chosen as the initial concentration for the experiments.

3.2.4 Adsorption kinetics, isotherms, and thermodynamic modeling. The adsorption kinetics of the MgCo-3D hydrotalcite nanospheres were investigated based on the results of batch adsorption experiments. Briefly, 0.01 g of the adsorbent was placed in 30 mL of 4-NP solution, and the adsorption capacity at different contact times was recorded for subsequent analysis. The adsorption kinetics were investigated using two models, namely the pseudo-first-order and pseudo-second-order models. The adsorption of 4-NP on the material was modeled using the Langmuir and Freundlich isotherm models, and the thermodynamic parameters were determined.

In this paper, the pseudo-first-order, pseudo-second-order kinetic models and intraparticle diffusion kinetic model are fitted.[42] Fig. 5(a–c) shows that the adsorption kinetics of 4-NP were inconsistent with the pseudo-first-order model and intra-particle diffusion kinetic model. In intraparticle diffusion kinetic model, if the fitting curve exhibits good linearity and passes through the origin, then adsorption was controlled by an intraparticle diffusion process. However, if the fitting curve did not pass through the origin, then a film diffusion process was the rate controlling step. As shown in Fig. 5(c), the lines did not pass through the origin, indicating the adsorption process of MgCo-3D hydrotalcite to 4-NP was controlled by a film diffusion mechanism.[43]

Fig. 5(b) shows that the adsorption kinetics of 4-NP were more consistent with the pseudo-second-order model, as the correlation coefficients for this model were greater than 0.99 at different temperatures (Table 2). The pseudo-second-order kinetic models of the adsorption rate, k_2, appears to increase with increasing ambient temperature of the 4-NP solution. As a result, the rate of adsorption reaction also increases. Consequently, the pseudo-second-order kinetic constants were used to calculate the activation energy of adsorption (E_a).[44] E_a of the MgCo-3D hydrotalcite nanospheres was 29.4 kJ mol^{-1} (less than 30 kJ mol^{-1}), which is typical of physical adsorption.
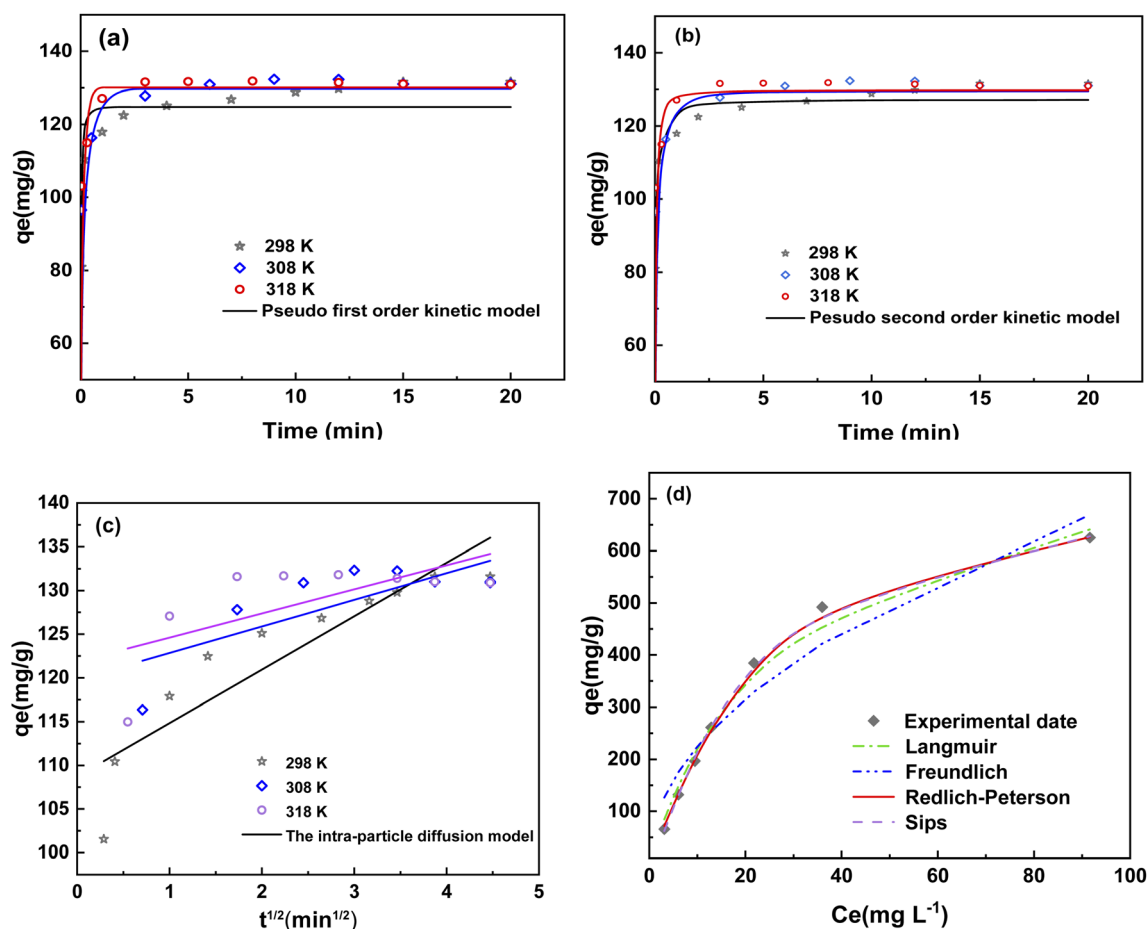

Fig. 5 (a, b and c) Fits to the pseudo-first-order, pseudo-second-order kinetic models and the intra-particle diffusion model at 298 K, 308 K and 318 K for the adsorption of 4-NP on MgCo-3D hydrotalcite nanospheres. (d) Adsorption isotherm at 298 K and fits to the Langmuir and Freundlich models for the adsorption of 4-NP on MgCo-3D hydrotalcite nanospheres (Ce (mg g^{-1}) is the 4-NP concentration in the solution at equilibrium).

Table 2 Fitting parameters of the pseudo-first-order and pseudo-second-order kinetic adsorption models for 4-NP

Models	298 K	308 K	318 K
Pseudo-first-order kinetic model			
k_1 (min^{-1})	26.30	33.24	33.15
$q_{e1,cal}$ (mg g^{-1})	124.75	129.67	130.08
$q_{e1,exp}$ (mg g^{-1})	131.59	131.01	130.09
R^2	0.9671	0.9804	0.9665
Pseudo-second-order kinetic model			
K_2 (g mg^{-1} min^{-1})	0.38	0.64	0.82
$q_{e2,cal}$ (mg g^{-1})	127.16	129.50	129.74
q_{e2exp} (mg g^{-1})	131.59	131.01	130.09
R^2	0.9919	0.9913	0.9905
The intra-particle diffusion model			
k_{ip} (mg g^{-1} min$^{1/2}$)	6.11	3.04	2.76
C	108.72	119.80	121.85
R^2	0.7997	0.4369	0.3443

Fig. 5(d) and Table 3 indicate a better fit of the adsorption data to the Langmuir model ($R^2 = 0.992$), Redlich–Peterson ($R^2 = 0.999$) and Sips models ($R^2 = 0.999$) than the Freundlich model ($R^2 = 0.934$). It can be seen from the Fig. 4(d) and Table 3 that the fitting coefficient is high and can be used to describe the adsorption behavior of 4-NP. The value of $K_L = 0.03$ in the Langmuir model indicated that the adsorption of MgCo-3D hydrotalcite nanospheres on 4-NP was a single-molecule spontaneous process with a relatively uniform distribution of the homogeneous active centers. Redlich–Peterson and Sips models are the combination of Langmuir and Freundlich models.[45] In

Table 3 Parameters of 4-NP adsorption on MgCo-3D hydrotalcite nanospheres based on the fits to the Langmuir and Freundlich adsorption isotherms

Models	298 K	308 K	318 K
Langmuir			
q_m (mg g^{-1})	835.53	813.00	784.00
K_L (L mg^{-1})	0.04	0.03	0.03
R^2	0.9920	0.9957	0.9946
Freundlich			
$1/n$	0.48	0.49	0.49
K_F (mg^{1-n} g^{-1} L^{-n})	72.02	71.99	71.99
R^2	0.9345	0.9586	0.9095
Redlich–Peterson			
K_{RP} (L g^{-1})	23.57	27.93	28.82
α_{RP} (L mg^{-1})	0.01	0.05	0.06
β_{RP}	1.34	0.92	0.89
R^2	0.9990	0.9980	0.9960
Sips			
q_{max} (mg g^{-1})	709.97	871.89	824.49
K_S (L mg^{-1})	0.02	0.03	0.04
$1/n$	0.99	0.94	0.92
R^2	0.9990	0.9980	0.9960

Table 4 Calculated thermodynamic parameters of 4-NP adsorption on the MgCo-3D hydrotalcite nanospheres

T (K)	ΔG (kJ mol^{-1})	ΔH (kJ mol^{-1})	ΔS (J(k mol)$^{-1}$)
298.15	−7.64	82.37	49.69
308.15	−7.92		
318.15	−8.01		

the Redlich-Peterson models, β_{RP} coefficient is close to 1, it can be seen that the Redlich–Peterson model is close to the Langmuir model, which is single molecule adsorption. In the Sips models, $1/n$ represents the homogeneity of adsorbent. As can be seen from the table, $1/n$ is less than zero and the higher the temperature, the smaller the $1/n$, the better the homogeneity.

Table 4 lists the thermodynamic parameters of the adsorption of 4-NP. $\Delta G < 0$ indicates that the adsorption is a spontaneous exothermic process. The increase in $|\Delta G|$ with increasing temperature indicated increased spontaneity.

3.3 Adsorption mechanism

3.3.1 Active sites of adsorption. The XRD patterns of the MgCo-3D hydrotalcite nanospheres before and after 4-NP adsorption are shown in Fig. 1(a). The material retained its characteristic peaks before and after the adsorption, indicating that the crystal structure of the material remained intact. However, the 2 diffraction peaks at $2\theta = 37°$ and $51°$, corresponding to Mg(OH)$_2$, weakened (Fig. 1(a)). Mg(OH)$_2$ was most likely covered by 4-NP, resulting in the weakened peak intensity.

To further confirm the active adsorption sites, XPS analysis of the adsorbent material was performed. The Co 2p spectrum showed that the Co^{3+}/Co^{2+} ratio decreased from 0.68 to 0.51 before and after adsorption, respectively, and that the amount of Co^{3+} decreased during the adsorption. A large amount of high-valent Co^{3+} in the adsorbent before adsorption renders the adsorbent surface positive, facilitating the adsorption of many 4-NP molecules to balance the charge. This leads to the coverage of Co^{3+}. The Co^{3+} peaks hift to lower binding energies (from 779.9 eV, 796.16 eV to 779.73, 795.57 eV), indicating that the electrons of 4-NP overlap with the outer electrons of Co^{3+}, leading to an increase in the outer electron density and an enhanced shielding effect. The Mg 1s spectrum could be deconvoluted into two peaks: Mg–O (1303.33 eV) and Mg–OH (1302.76 eV). Both the peaks are attributed to the Mg in the hydromagnesite-like layer of the LDH. Adsorption of 4-NP results in a decrease in the Mg–OH peak intensity and a shift toward lower binding energies, suggesting the interaction of Mg–OH with 4-NP and an increased charge density. Analysis of the Co 2p and Mg 1s spectra showed that the adsorption centers of the MgCo-3D hydrotalcite nanospheres were Mg^{2+} and Co^{3+}, both of which are present in the hydrotalcite structures.[46–48] This demonstrates that hydrotalcite plays a major role in adsorption.

3.3.2 Electrostatic interactions. The pKa of 4-NP is 7.15, and it is mainly present in the solution as ions (4-NP, pH > 7.15) and molecules (4-NP, pH < 7.15).[49] Zeta potential analysis
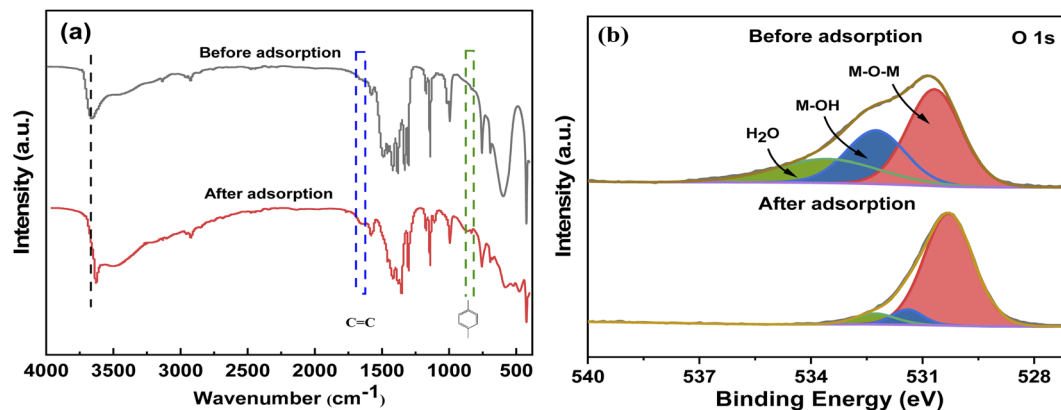
Fig. 6 (a) FT-IR spectra of the MgCo-3D hydrotalcite nanospheres before and after adsorption. (b) O 1s XPS fine spectrum of the MgCo-3D hydrotalcite nanospheres before and after adsorption.

(Fig. 4(b)) showed that the adsorbent surface was always positive. When the pH was increased from 3 to 7, the OH^- concentration in the solution increased, protonation of the LDH layer hydroxyls weakened, active sites were gradually exposed, and adsorption capacity gradually increased. When the pH was further increased from 7 to 13, 4-NP was mainly present in the anionic form (4-NP), We believe that 4-NP has electrostatic interaction with the electropositive surface of the adsorbent.[50] When the pH increases, the adsorption capacity did not increase further because the zeta potential of the adsorbent decreased, accompanied by the competition from OH^- ions in water for adsorption.

3.3.3 Hydrogen bonding. To elucidate the adsorption mechanism of 4-NP, the FT-IR spectrum of the MgCo-3D hydrotalcite nanospheres was analyzed. Fig. 6(a) shows the FT-IR spectra of the pristine and loaded adsorbents. The functional groups remained essentially the same before and after

adsorption, indicating that the material structure was not damaged during adsorption.[51] The peak at 425 cm^{-1} corresponds to the unique Co–N bending vibration. The peak at 2920 cm^{-1} can be attributed to the antisymmetric C–H stretching vibration, that at 1579 cm^{-1} can be attributed to the in-plane C=N bending vibration,[52] and those at 694, 756, and 1140–1500 cm^{-1} can be attributed to the bending and stretching vibrations of imidazole.[26] The MgCo-3D hydrotalcite nanospheres exhibited some new peaks after adsorption. The peak at 832 cm^{-1} corresponds to the para-substituted benzene ring of 4-NP; however, the intensity of the peak is low, which can be attributed to the low concentration of 4-NP in the sample. The peak at 1640 cm^{-1} corresponds to the C=C stretching vibration in the benzene ring of 4-NP. Both these facts confirm the adsorption of 4-NP on the hydrotalcite surface. The –OH absorption band shifted from 3660 cm^{-1} (before adsorption) to 3630 cm^{-1} (after adsorption), indicating the formation of

Table 5 Binding energy and relative content of Co 2p, ad Mg 1s in the MgCo-3D hydrotalcite before and after adsorption

			Before adsorption		After adsorption	
		Species	Binding energy (eV)	Atom%	Binding energy (eV)	Atom%
Co 2p	$2p_{3/2}$	Co^{2+}	781.50	32.89	780.79	35.70
		Co^{3+}	779.90	20.72	779.73	17.86
	$2p_{1/2}$	Co^{2+}	797.33	10.20	796.38	13.21
		Co^{3+}	796.16	8.55	795.57	7.14
Mg 1s	Mg–O		1303.33	36.71	1302.51	62.89
	Mg–OH		1302.76	63.29	1302.01	37.11

Table 6 Binding energies and relative O 1s contents of the MgCo-3D hydrotalcite before and after adsorption

		Before adsorption		After adsorption	
Species		Binding energy(eV)	Atom%	Binding energy(eV)	Atom%
O 1s	M-O-M	530.88	63.29	530.38	89.23
	M-OH	532.68	28.96	531.58	8.40
	H_2O	534.68	7.75	532.95	2.37

hydrogen bonds (Table 5). Since oxygen atoms are more electronegative than nitrogen atoms, hydrogen bonds are more likely to form with the former. M–OH likely forms hydrogen bonds with –OH and –NO$_2$.[53]

The C 1s XPS spectrum changed before and after adsorption. The peak position, peak intensity, and the increase in peak intensity indicated that 4-NP was successfully adsorbed onto the MgCo-3D hydrotalcite nanospheres. Fig. 6(b) shows the O 1s spectrum. The binding energy corresponding to the O 1s peak decreased significantly from 531.33 to 530.84 eV after the adsorption. The peaks at 530.68 and 532.25 eV corresponded to M–O–M (Mg–O–Co) and M–OH (Mg–OH, Co–OH), respectively, while the peak at 533.55 eV can be attributed to adsorbed water molecules. After adsorption (Fig. 6(b)), although the OH groups in 4-NP should increase the total fraction of the hydroxyl groups, the adsorbed M–OH content decreased from 28.96% to 8.40%. M–OH should be covered by 4-NP molecules (Table 6). However, the M–O–M content increased from 63.29% to 89.23%, indicating that the hydroxyl group was involved in the adsorption of 4-NP on the MgCo-3D hydrotalcite nanospheres.[54]

The mechanism of adsorption of 4-NP on the MgCo-3D hydrotalcite nanospheres is shown in Fig. 7. The Fig. 7 shows that 4-NP is adsorbed on MgCo-3D hydrotalcite nanospheres through hydrogen bonding and electrostatic forces. Our results suggest that the unsaturated metal sites in the MgCo-3D hydrotalcite nanospheres and the coulombic interactions (through hydrogen bonding) are the main driving forces of adsorption. During the adsorption of 4-NP pairs on the MgCo-3D hydrotalcite nanospheres, the unsaturated metal (Mg and Co) sites in the MgCo-3D hydrotalcite nanospheres were coordinated with the nitro group in 4-NP. The hydroxyl group on the adsorbent surface was hydrogen-bonded to the hydroxyl group or nitro group of 4-NP, facilitating its adsorption on the surface of the MgCo-3D hydrotalcite nanospheres and improving its adsorption efficiency. In addition, the adsorption efficiency increased with increasing pH (up to pH 7) owing to the positive charge on the adsorbent surface, and this increased the attractive forces between the adsorbent and phenol ions.
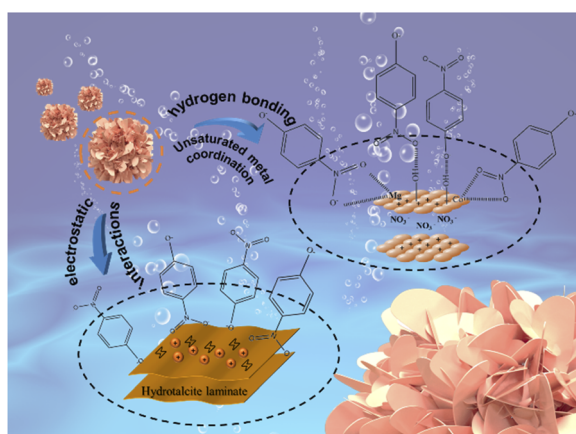

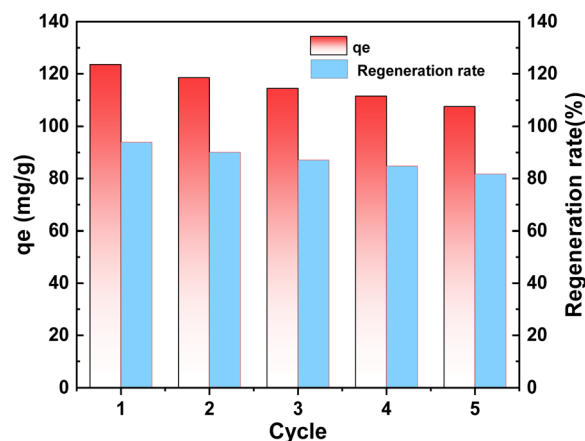**Fig. 7** Adsorption mechanism of 4-NP on the MgCo-3D hydrotalcite nanospheres.

Fig. 8 Adsorption capacity and regeneration efficiency of the MgCo-3D hydrotalcite nanospheres after adsorption–desorption cycles.

4. Regeneration

In practical scenarios, the regeneration performance of an adsorbent determines its successful commercial application. In this study, the adsorbent was regenerated by hot-air purging.[55] The supernatant of the adsorbate-saturated MgCo-3D hydrotalcite nanospheres was separated *via* centrifugation to obtain a solid adsorbent, which was placed in a crucible and regenerated by air purging at 180 °C and 4 L min^{-1} for 4 h. Five adsorption–desorption cycle regeneration tests were performed (Fig. 8). The adsorption capacity decreased from 131.59 to 107.6 mg g^{-1}, and the regeneration efficiency was 81.76% in the fifth cycle. This indicated good regeneration performance and hence great application potential.

5. Conclusion

(1) The maximum adsorption amount was 131.59 mg g^{-1} at pH = 7, T = 298 K, C_0 = 50 mg L^{-1}, and dose = 0.4 g L^{-1}. The adsorption followed pseudo-second-order kinetics and was consistent with the Langmuir model, Redlich–Peterson and Sips models isothermal adsorption model. The activation energy of adsorption was 29.4 kJ mol^{-1}, indicating single-molecule physical adsorption.

(2) The chemical and structural changes in the MgCo-3D hydrotalcite nanospheres before and after adsorption indicated that the adsorption of 4-NP was dominated by hydrogen bonding and electrostatic interactions.

(3) The regeneration efficiency was maintained at 81.76% after five adsorption–desorption cycles by hot air purging method, indicating that the adsorbent has good regeneration performance.

Conflicts of interest

There are no conflicts to declare.

References

1 S. Zhu, W. Niu, H. Li, *et al.* Single-walled carbon nanohorn as new solid-phase extraction adsorbent for determination of 4-nitrophenol in water sample, *Talanta*, 2009, **79**(5), 1441–1445.

2 F. M. M. Tchieno and I. K. Tonle, p-Nitrophenol determination and remediation: an overview, *Rev. Anal. Chem.*, 2018, **37**(2), 20170019.

3 G. Busca, S. Berardinelli, C. Resini, *et al.* Technologies for the removal of phenol from fluid streams: a short review of recent developments, *J. Hazard. Mater.*, 2008, **160**(2–3), 265–288.

4 J. C. Lazo-Cannata, A. Nieto-Márquez, A. Jacoby, *et al.* Adsorption of phenol and nitrophenols by carbon nanospheres: Effect of pH and ionic strength, *Sep. Purif. Technol.*, 2011, **80**(2), 217–224.

5 T. V. Tran, T. D. Nguyen, Q. Bui, *et al.* Efficient removal of Ni^{2+} ions from aqueous solution using activated carbons fabricated from rice straw and tea waste, *Indian J. Eng. Mater. Sci.*, 2016, **8**(2), 426–437.

6 G. Wang, H. Xiao, J. Zhu, *et al.* Simultaneous removal of Zn^{2+} and p-nitrophenol from wastewater using nanocomposites of montmorillonite with alkyl-ammonium and complexant, *Environ. Res.*, 2021, **201**, 111496.

7 I. Pavlovic, M. Pérez and] C. Barriga, Removal of acid orange 10 by calcined Mg/Al layered double hydroxides from water and recovery of the adsorbed dye, *Chem. Eng. J.*, 2012, **213**, 392–400.

8 Y. Sun, J. Zhou, *et al.* Hierarchically porous NiAl-LDH nanoparticles as highly efficient adsorbent for p-nitrophenol from water, *Appl. Surf. Sci.*, 2015, **349**, 897–903.

9 A. Tacb, A. Crb and A. Adds, Preparation and evaluation of iron oxide/hydrotalcite intercalated with dodecylsulfate/β-cyclodextrin magnetic organocomposite for phenolic compounds removal, *Appl. Clay Sci.*, 2020, **193**, 105659.

10 N. Kumar, L. Reddy, V. Parashar, *et al.* Controlled synthesis of microsheets of ZnAl layered double hydroxides hexagonal nanoplates for efficient removal of Cr(VI) ions and anionic dye from water, *J. Chem. Environ. Eng.*, 2017, **5**(2), 1718–1731.

11 R. Li, R. Che, Q. Liu, *et al.* Hierarchically structured layered-double-hydroxides derived by ZIF-67 for uranium recovery from simulated seawater, *J. Hazard. Mater.*, 2017, **338**, 167–176.

12 X. Wang, W. Zhou, C. Wang, *et al.* Cotton fiber supported layered double hydroxides for highly efficient adsorption of anionic organic pollutants in water, *New J. Chem.*, 2018, **42**(12), 9463–9471.

13 I. Ihsanullah, Applications of MOFs as adsorbents in water purification: Progress, challenges and outlook, *Curr. Opin. Environ. Sci. Health*, 2022, **26**, 100335.

14 S. Ahmadi, M. R. Kalaee, O. Moradi, *et al.* Synthesis of novel zeolitic imidazolate framework (ZIF-67) - zinc oxide (ZnO) nanocomposite (ZnO@ZIF-67) and potential adsorption of pharmaceutical (tetracycline (TCC)) from water, *J. Mol. Struct.*, 2022, 1251.

15 H. Lgaz and H.-S. Lee, Computational investigation on interaction mechanism of sulfur mustard adsorption by zeolitic imidazolate frameworks ZIF-8 and ZIF-67: Insights from periodic and cluster DFT calculations, *J. Mol. Liq.*, 2021, **344**, 117705.

16 H. Miao, S. Song, H. Chen, *et al.* Adsorption study of p-nitrophenol on a silver(I) triazolate MOF, *J. Porous Mater.*, 2020, **27**, 1049–1417.

17 A. M. Aldawsari, I. H. Alsohaimi, H. M. Hassan, *et al.* Activated carbon/MOFs composite: AC/NH2-MIL-101 (Cr), synthesis and application in high performance adsorption of p-nitrophenol, *J. Saudi Chem. Soc.*, 2020, **24**(9), 693–703.

18 K.-Y. A. Lin and Y.-T. Hsieh, Copper-based metal organic framework (MOF), HKUST-1, as an efficient adsorbent to remove p-nitrophenol from water, *J. Taiwan Inst. Chem. Eng.*, 2015, **50**, 223–228.

19 A. Myz, A. Czf, A. Xfy, *et al.* Promoting Ni-MOF with metallic Ni for highly-efficient p-nitrophenol hydrogenation, *Mol. Catal.*, 2021, **509**, 111609.

20 S. Saghir, E. Fu and Z. Xiao, Synthesis of CoCu-LDH nanosheets derived from zeolitic imidazole framework-67 (ZIF-67) as an efficient adsorbent for azo dye from waste water, *Microporous Mesoporous Mater.*, 2020, **297**, 110010.

21 M. A. Nazir, N. A. Khan, C. Cheng, *et al.* Surface induced growth of ZIF-67 at Co-layered double hydroxide: Removal of methylene blue and methyl orange from water, *Appl. Clay Sci.*, 2020, **190**, 105564.

22 D. Wang, S. Li, Y. Du, *et al.* Self-Templating Synthesis of 3D Hierarchical NiCo2O4@NiO Nanocage from Hydrotalcites for Toluene Oxidation, *Catalysts*, 2019, **9**(4), 352.

23 C. Hao, X. Wang and X. Wu, Composite material CCO/Co-Ni-Mn LDH made from sacrifice template CCO/ZIF-67 for high-performance supercapacitor, *Appl. Surf. Sci.*, 2022, **572**, 151373.

24 Q. Wang, X. Wang, H. He, *et al.* ZIF-67 derived hollow OCS/NiCo-LDH nanocages as binder-free electrodes for high performance supercapacitors, *Appl. Clay Sci.*, 2020, **198**, 105820.

25 T. B. Nguyen, V. A. Thai, C. W. Chen, *et al.* N-doping modified zeolitic imidazole Framework-67 (ZIF-67) for enhanced peroxymonosulfate activation to remove ciprofloxacin from aqueous solution, *Sep. Purif. Technol.*, 2022, **288**, 120719.

26 J.-W. Zhang, A. D. Nur'aini, Y.-C. Wang, *et al.* Multiple pollutants removal by carbon sphere and layered double hydroxide composites: Adsorption behavior and mechanisms, *J. Chem. Environ. Eng.*, 2022, **10**(3), 108014.

27 W. A. Xing, C. A. Bei and B. Lz, Synthesis of MgNiCo LDH hollow structure derived from ZIF-67 as superb adsorbent for Congo red, *J. Colloid Interface Sci.*, 2022, **612**, 598–607.

28 O. Amrhar, L. El Gana and M. Mobarak, Calculation of adsorption isotherms by statistical physics models: a review, *Environ. Chem. Lett.*, 2021, **19**(6), 4519–4547.

29 R. Bardestani, G. S. Patience and S. Kaliaguine, Experimental methods in chemical engineering: specific surface area and pore size distribution measurements—BET, BJH, and DFT, *Can. J. Chem. Eng.*, 2019, **97**(11), 2781–2791.

30 S. Mishra, S. S. Yadav, S. Rawat, *et al.* Corn husk derived magnetized activated carbon for the removal of phenol and para-nitrophenol from aqueous solution: Interaction mechanism, insights on adsorbent characteristics, and isothermal, kinetic and thermodynamic properties, *J. Environ. Manag.*, 2019, **246**, 362–373.

31 T. a C. Balbino, C. R. Bellato, A. D. Da Silva, *et al.* Preparation and evaluation of iron oxide/hydrotalcite intercalated with dodecylsulfate/β-cyclodextrin magnetic organocomposite for phenolic compounds removal, *Appl. Clay Sci.*, 2020, **193**, 105659.

32 B. Liu, T. Chen, B. Wang, *et al.* Enhanced Removal of Cd^{2+} From Water by AHP-pretreated Biochar: Adsorption Performance and Mechanism, *J. Hazard. Mater.*, 2022, 129467.

33 S. Mohammadi, Phenol Removal from Industrial Wastewaters: A Short Review, *ChemInform*, 2015, **46**(12), 2215–2234.

34 R. Li, R. Che, Q. Liu, *et al.* Hierarchically structured layered-double-hydroxides derived by ZIF-67 for uranium recovery from simulated seawater, *J. Hazard. Mater.*, 2017, **338**, 167–176.

35 H. Zheng, W. Guo, S. Li, *et al.* Adsorption of p-nitrophenols (PNP) on microalgal biochar: analysis of high adsorption capacity and mechanism, *Bioresour. Technol.*, 2017, **244**, 1456–1464.

36 H. Zeng, W. Lu, L. Hao, *et al.* Adsorptive removal of p-nitrophenol from water with mechano-synthesized porous organic polymers, *New J. Chem.*, 2018, **42**(24), 20205–20211.

37 M. Saber S E, L. C. Abdullah, S. N. a M. Jamil, *et al.* Trimethylamine functionalized radiation-induced grafted polyamide 6 fibers for p-nitrophenol adsorption, *Sci. Rep.*, 2021, **11**(1), 19573.

38 Z. Jia, M. Jiang and G. Wu, Amino-MIL-53 (Al) sandwich-structure membranes for adsorption of p-nitrophenol from aqueous solutions, *Chem. Eng. J.*, 2017, **307**, 283–290.

39 S. F. N. Khomeyrani, B. Ghalami-Choobar, M. H. A. Azqhandi, *et al.* An enhanced removal of para-nitrophenol (PNP) from water media using CaAl-layered double hydroxide-loaded magnetic g-CN nanocomposite, *J. Water Proc. Eng.*, 2022, 102516.

40 H.-M. Shen, G.-Y. Zhu, W.-B. Yu, *et al.* Surface immobilization of β-cyclodextrin on hybrid silica and its fast adsorption performance of p-nitrophenol from the aqueous phase, *RSC Adv.*, 2015, **5**(103), 84410–84422.

41 Y. Park, G. A. Ayoko, R. Kurdi, *et al.* Adsorption of phenolic compounds by organoclays: Implications for the removal of organic pollutants from aqueous media, *J. Colloid Interface Sci.*, 2013, **406**, 196–208.

42 Y.-S. Ho, Review of second-order models for adsorption systems, *J. Hazard. Mater.*, 2006, **136**(3), 681–689.

43 X. Zeng, G. Zhang and J. Zhu, Selective adsorption of heavy metals from water by a hyper-branched magnetic composite material: Characterization, performance, and mechanism, *J. Environ. Manage.*, 2022, **314**, 114979.

44 N. Soliman, A. Moustafa, H. Abd El-Mageed, *et al.* Experimentally and theoretically approaches for disperse red 60 dye adsorption on novel quaternary nanocomposites, *Sci. Rep.*, 2021, **11**(1), 1–27.

45 M. P. Da Rosa, A. V. Igansi, S. F. Lütke, *et al.* A new approach to convert rice husk waste in a quick and efficient adsorbent to remove cationic dye from water, *J. Chem. Environ. Eng.*, 2019, **7**(6), 103504.

46 Z. Liu, Y. Zhong, Y. Qiu, *et al.* Multilayered and hierarchical structured NiCo double hydroxide nanosheets generated on porous $MgCo_2O_4$ nanowire arrays for high performance supercapacitors, *Appl. Surf. Sci.*, 2021, **546**, 149133.

47 K. Rybka, J. Matusik, A. Kuligiewicz, *et al.* Surface chemistry and structure evaluation of Mg/Al and Mg/Fe LDH derived from magnesite and dolomite in comparison to LDH obtained from chemicals, *Appl. Surf. Sci.*, 2021, **538**, 147923.

48 F. Zhang, C.-L. Zhang, L. Song, *et al.* Corrosion resistance of superhydrophobic Mg–Al layered double hydroxide coatings on aluminum alloys, *Acta Metall. Sin.*, 2015, **28**(11), 1373–1381.

49 H. Miao, S. Song, H. Chen, *et al.* Adsorption study of p-nitrophenol on a silver (I) triazolate MOF, *J. Porous Mater.*, 2020, **27**(5), 1409–1417.

50 R. Gerhardt, B. S. Farias, J. M. Moura, *et al.* Development of chitosan/Spirulina sp. blend films as biosorbents for Cr^{6+} and Pb^{2+} removal, *Int. J. Biol. Macromol.*, 2020, **155**, 142–152.

51 J. Hu, G. Zhao, X. Long, *et al.* In situ topotactic fabrication of ZnS nanosheet by using ZnAl-layered double hydroxide template for enhanced tetracycline pollutant degradation activity, *Mater. Sci. Semicond. Process.*, 2021, **134**, 106007.

52 X. Wu, X. Wang, Y. Hu, *et al.* Adsorption mechanism study of multinuclear metal coordination cluster Zn5 for anionic dyes Congo red and methyl orange: Experiment and molecular simulation, *Appl. Surf. Sci.*, 2022, **586**, 152745.

53 S. A. Khan, E. M. Bakhsh, K. Akhtar, *et al.* A template of cellulose acetate polymer-ZnAl/C layered double hydroxide composite fabricated with Ni NPs: Applications in the hydrogenation of nitrophenols and dyes degradation, *Spectrochim. Acta, Part A*, 2020, **241**, 118671.

54 J. Li, Y.-N. Wu, Z. Li, *et al.* Zeolitic imidazolate framework-8 with high efficiency in trace arsenate adsorption and removal from water, *J. Phys. Chem. C*, 2014, **118**(47), 27382–27387.

55 W. Teng, N. Bai, Z. Chen, *et al.* Hierarchically porous carbon derived from metal-organic frameworks for separation of aromatic pollutants, *Chem. Eng. J.*, 2018, **346**, 388–396.